Supplementary Information

In situ Assembled WO_3-TiO_2 Vertical Heterojunction for Enhanced Z-scheme Photocatalytic Activity

Yue Liu, Xiangkang Zeng, Christopher D. Easton, Qinye Li, Yun Xia, Yichun Yin, Xiaoyi Hu, Jian Hu, Dehua Xia, David T. McCarthy, Ana Deletic, Chenghua Sun, Jiaguo Yu and Xiwang Zhang*

*Corresponding Author: xiwang.zhang@monash.edu

Sections

Experimental Section

X-ray photoelectron spectroscopy (XPS) characterization

a) XPS methodology employed in this study

b) Experimental Details

c) Quantification

d) Measured binding energy shifts in high-resolution spectra - Charge correction

e) Influence of in situ assembly for heterojunction formation and light irradiation on peak positions

f) Details regarding the fitting of W 4f spectra

g) Results from fitting W 4f spectra – influence of the in situ assembly and in situ UV irradiation

Table S1. XPS spin orbital component positions for selected elements from high-resolution spectra for samples without irradiation.

Table S2. XPS spin orbital component positions for selected elements from high-resolution spectra for samples with irradiation.

Table S3. Relative fraction of W species in WO_3 and WO_3-TiO_2 heterojunction samples derived from component fitting of high-resolution W 4f XPS spectra.

Fig. S1 Selected, representative high-resolution O 1s spectra from TiO_2, WO_3 and WO_3-TiO_2 heterojunction samples

Fig. S2 Selected, representative high-resolution Ti 3p spectrum from the TiO_2 reference sample

Fig. S3 Fitting of selected, representative W 4f spectra of the WO_3-TiO_2 heterojunction with irradiation using a model spectrum.

Characterization of the WO_3-TiO_2 heterojunction

Fig. S4 TEM image of TiO_2 nanosheets synthesized by the growth control method.

Z-scheme photocatalytic charge transportation route

Photocatalytic antibacterial performance

References

Experimental Section

X-ray photoelectron spectroscopy (XPS) characterization

a) XPS methodology employed in this study

Below is a detailed description of the steps involved in the acquisition, processing and interpretation of the XPS data collected for this study. This is provided so that the reader has sufficient information to replicate this study and can judge the validity of the results presented. The reasoning for providing a detailed account is threefold:

1) It is in direct response to what has been coined the "reproducibility crisis", where there is great concern regarding reproducibility and replication issues in science in general, but more specifically the impact in vacuum sciences,[1] which includes XPS. As detailed by Baer and Gilmore,[1] there is a coordinated effort by those in the field to address this problem; this section has been written for this purpose.

2) Use of XPS in the characterisation of materials for catalysis has been common for many years. However, after a limited review of the literature of the field, it is apparent that insufficient detail is provided for XPS experimentation and interpretation. For example, studies that have reported observing charge transfer in photocatalysts with XPS don't tend to provide any detail on their methodology for charge correction. Thus, we hope to provide readers with sufficient information such that they can reproduce our experimentation and to encourage best practice.

3) The conclusions derived in this work rely heavily on the XPS data and interpretation.

b) Experimental Details

XPS analysis was performed using AXIS Nova and AXIS Ultra-DLD spectrometers (Kratos Analytical Inc., Manchester, UK) with a monochromated Al Kα source at a power of 180 W

(15 kV 12 mA) and a hemispherical analyser operating in the fixed analyser transmission mode. The total pressure in the main vacuum chamber during analysis was typically between 10^{-9} and 10^{-8} mbar. Survey spectra were acquired at a pass energy of 160 eV. To obtain more detailed information about chemical structure, oxidation states etc., high-resolution spectra were recorded from individual peaks at 20 eV (yielding a typical peak width for polymers of < 1.0 eV).

Every specimen was analysed at an emission angle of 0° as measured from the surface normal. Assuming typical values for the electron attenuation length of relevant photoelectrons the XPS analysis depth (from which 95 % of the detected signal originates) ranges between 5 and 10 nm for a flat surface.

In situ UV irradiation of the sample, where the sample is irradiated during XPS analysis, was performed using a helium discharge source optimised for He I radiation (21.22 eV), normally employed for Ultraviolet Photoelectron Spectroscopy (UPS). To confirm operation of the lamp and alignment of illumination with the sample surface, a UPS spectrum was collected from an Ag foil sample etched with a Gas Cluster Ion Source (Minibeam 6) for at least 60s. During in situ irradiation of the WO_3, TiO_2 and WO_3-TiO_2 heterojunction samples, only high-resolution spectra were collected. Data collection near the Fermi edge using the parameters employed herein was prevented to avoid saturating the detector with UV-photoelectrons and thus ensure the integrity of the analyser.

c) Quantification

Data processing was performed using CasaXPS processing software version 2.3.15 (Casa Software Ltd., Teignmouth, UK). All elements present were identified from survey spectra. The atomic concentrations of the detected elements were calculated using integral peak intensities and the sensitivity factors supplied by the manufacturer.

The accuracy associated with quantitative XPS is *ca.* 10% - 15%.

Precision (*i.e.* reproducibility) depends on the signal/noise ratio but is usually much better than 5%. The latter is relevant when comparing similar samples.

d) Measured binding energy shifts in high-resolution spectra - Charge correction

When comparing peak positions of high-resolution XPS spectra, a reliable and consistent charge correction methodology is necessary. It is important to detail the methodology used for charge correction when presenting such comparisons, particularly when an author relies heavily on minor changes in binding energy (BE), so that the reader can make a judgement call regarding the validity of the statements made based on these shifts. In this work, we used BE positions to compare the position of peaks of the reference WO_3 and TiO_2, and the WO_3-TiO_2 heterojunction; we also compare the peak positions of the samples without and during in situ irradiation. The error associated with charge correction is approximately ± 0.2 eV;[2] as a result, minor shifts in BE between spectra that are sometimes relied upon in the literature can be insignificant and thus readers should take care when interpreting and relying upon such results.

Several attempts were made to find the most appropriate peak and BE for charge correction of these samples. It was decided to reference BEs to the C 1s peak at 285 eV, which would be consistent with aliphatic hydrocarbon. It is acknowledged that the C 1s is not the most appropriate peak for charge reference for inorganic samples, where it is usually associated with adventitious carbon and in low concentration. A discussion of the merits of using adventitious carbon as a charge reference can be found elsewhere.[2, 3] Nevertheless, it became apparent while processing the data that there was no other peak available for charge correction, as it was observed that the peak position of some peaks in the heterojunction shifted relative to the reference materials. Such a result would be consistent with charge sharing between different components of the nanocomposite.

Peak positions for the samples without and during in situ irradiation are provided below in **Table S1** and **Table S2**. In the case of the WO_3 and TiO_2 reference materials, the peak positions are consistent with reference data found in the NIST database[4] and other published results.[5, 6] Thus, charge correction of the spectra to the C 1s peak at 285 eV was considered satisfactory in this case.

e) Influence of in situ assembly for heterojunction formation and light irradiation on peak positions

For the WO_3-TiO_2 heterojunction, the O 1s peak position is consistent with the measured value for the reference WO_3 sample rather than the reference TiO_2 sample (**Fig. S1**). No evidence of differential charging was observed (*i.e.* shifting of part of the peak intensity to higher BEs) in the O 1s spectra, or any other spectra examined herein. In all cases, the majority of intensity for O 1s was assigned to oxygen associated with oxide at 529.7 ± 0.1 for TiO_2 or 530.6 ± 0.1 for WO_3 and the heterojunction.

In regards to the W $4f_{7/2}$ peak, a difference of 0.06 eV was observed in the BE position when comparing the WO_3 reference and WO_3-TiO_2, with a shift to lower BE for WO_3-TiO_2. Based on the discussion above, the magnitude of the shift is not considered significant, though a shift to lower BE would be consistent with W accepting electrons.

The only significant shift observed is that of the Ti $2p_{3/2}$ peak. For the WO_3-TiO_2, a BE of 459.4 ± 0.1 eV was measured, equating to a shift of +0.9 eV relative to the TiO_2 reference sample. A positive shift in peak position is consistent with Ti donating electrons. Thus the shifts in the WO_3-TiO_2 peak positions relative to the starting materials suggest that the TiO_2 in the heterojunction is donating electrons to WO_3.

For all elements and species examined here, no significant shift was observed in binding energy when the samples were irradiated with the He lamp discharge. The largest shift recorded was less than 0.1 eV as shown in **Table S2**.

f) Details regarding the fitting of W 4f spectra

Fitting of high-resolution XPS spectra, in particular mixed metal and metal oxide spectra, is not trivial. Thorough knowledge of the core principles underpinning the photoemission process, in addition to an understanding of the instrumentation and experimental procedure are necessary to first design the appropriate experiment, then process and interpret the resultant data correctly. In the best case scenario, researchers should rely on independent subject matter experts to assist with processing and interpreting XPS spectra. Collaboration with facilities with such expertise is strongly encouraged. If such expertise is not available, then researchers should rely on resources such as credible books,[7, 8] online resources[9, 10] and specialist journals such as Surface Science Spectra to build expertise. It is not recommended that researches rely solely on research articles in their specialised field. This section is aimed at a reader with experience in peak fitting of XPS spectra using a software package such as CasaXPS and an understanding of the core principals behind XPS.

Recently, Peter M.A. Sherwood published an excellent review article that explores fundamental aspects and many of the complications involved in fitting of XPS spectra.[6] Sherwood provides a detailed overview of the history of fitting functions employed in the field, where the author states "The Voigt function is preferred to the pseudo Voigt functions as it is the most physically meaningful function".[6] Within CasaXPS, pseudo-Voight functions are represented by GL and SGL line-shapes which are commonly used in the literature but not recommended, while the LA and LF line-shapes represent a generalised Voigt line-shape.[11] Herein, the following LF line-shapes were employed for the specified spin orbital components: O 1s - LF(0.8,1.2,30,400); W 5p - LF(1,1.5,10,200); W 4f - LF(1,1.8,100,200).

In addition to line-shapes, another important but often overlooked parameter of a fit is the choice of background. Details of various background types can be found elsewhere.[6, 11] It is of this author's opinion that choice of background is a contentious issue in the field and there is

no clear "one size fits all" approach to selection, nor is there a consensus regarding the best approach. Herein, a three-parameter Tougaard background was employed for all peak fitting;[12] application of this background as "U 3 Tougaard" within CasaXPS can be found elsewhere.[13]

To account for spin orbital splitting of the W 4f peak, two components were employed to represent W $4f_{7/2}$ and W $4f_{5/2}$, where each doublet is assigned to a specific W species. A fixed area ratio of 4:3 was employed for each doublet. Initially, a fixed doublet separation was employed. However, an improved figure of merit was obtained when then the position of the W $4f_{5/2}$ peak was allowed some freedom of movement via a small window in the position constraint for the fit. In both the WO_3 reference and WO_3-TiO_2 heterojunction, a shoulder was observed at the lower BE side of the W 4f spectra, for example, **Fig. S17** and **Fig. 4**f-g When fitting the W 4f spectra, the majority of the intensity was assigned to W^{6+}, while the shoulder was assigned to W^{5+}. A peak was observed at higher BE associated with W 5p and was represented by a single component. In the case of WO_3-TiO_2, an additional component was required to account for the intensity associated with the Ti 3p peak that overlaps with the W 4f peak. For this component, a Ti 3p spectrum collected from the TiO_2 reference sample as shown in **Fig. S2** was used as a model component. Fitting spectra using model components has been utilized previously in the literature.[14]

g) Results from fitting W 4f spectra – influence of the in situ assembly and in situ UV irradiation

Results from fitting of the W 4f spectra are presented in **Table S3**, where representative spectra can be found in **Fig. S17** and **Fig. 4**f-g. The influence of in situ coupling on the W 4f spectra was observed in the concentration of the component doublet assigned to W^{5+} with a measured change in %Area of 144.7%. The heterojunction had the largest measured relative fraction of W^{5+}, without and with irradiation. The measured changes in peak position detailed above, while not significant, were consistent with W accepting electrons, whereby an increase

in W^{5+} provides additional evidence for this hypothesis. For both WO_3 and the WO_3-TiO_2 heterojunction, an increase in the relative fraction of W^{5+} was observed with irradiation. The change in %Area of the component doublet was 43.0% for WO_3 and 23.0% for WO_3-TiO_2.

An alternative fitting protocol was employed for the W 4f spectrum of the heterojunction with irradiation, presented in **Fig. S3**. A spectrum of the WO_3-TiO_2 heterojunction without irradiation was used as a fitting component, where the full width at half maximum was fixed to a very narrow window (i.e. 1.0 ± 0.01) to accurately reflect the spectral envelope of a nanocomposite spectrum. The remainder of the intensity for the spectrum was accounted by a single doublet "W2", which was assigned to W^{5+} in all the fits presented herein. This fit demonstrates that with in situ UV light irradiation, the change in the W 4f spectrum is associated with a change in the relative fraction of the two main species W^{6+} and W^{5+}. It also confirms the result of the original fitting protocol that there is an increase in intensity associated of W^{5+} with irradiation. As the change in the peak shape of the W 4f spectrum is accounted solely by the W^{5+} component doublet with the fitting parameter restrictions detailed above, it is unlikely that the relative change in W^{5+} intensity is associated with an instrumental artefact, such as differential charging.

Table S1. XPS spin orbital component positions for selected elements from high-resolution spectra for **samples without irradiation**. Listed are the mean ± deviation from two analysis points per sample, with two (TiO_2 and WO_3 samples) or four (WO_3-TiO_2) samples per sample type.

Sample	**Measured binding energy values (eV)**						
	W 5p	**W $4f_{7/2}$**		**W $4f_{5/2}$**		**O 1s**	**Ti 2p**
		$W^{(6+)}$ – W1a	**$W^{(5+)}$ – W2a**	**$W^{(6+)}$ – W1b**	**$W^{(5+)}$ – W2b**		
TiO_2	-	-	-	-	-	529.7 ± 0.1	458.5 ± 0.0
WO_3	41.42 ± 0.10	35.79 ± 0.07	34.67 ± 0.08	37.94 ± 0.07	36.80 ± 0.08	530.6 ± 0.1	-
WO_3-TiO_2 heterojunction	41.36 ± 0.05	35.73 ± 0.04	34.67 ± 0.04	37.86 ± 0.04	36.70 ± 0.00	530.6 ± 0.1	459.4 ± 0.1

Table S2. XPS spin orbital component positions for selected elements from high-resolution spectra for **samples with irradiation**. Listed are the mean ± deviation from one analysis point per sample, with two (TiO_2 and WO_3 samples) or four (WO_3-TiO_2) samples per sample type.

Sample	**Measured binding energy values (eV)**						
	W 5p	**W $4f_{7/2}$**		**W $4f_{5/2}$**		**O 1s**	**Ti 2p**
		$W^{(6+)}$ – W1a	**$W^{(5+)}$ – W2a**	**$W^{(6+)}$ – W1b**	**$W^{(5+)}$ – W2b**		
TiO_2	-	-	-	-	-	529.7 ± 0.1	458.5 ± 0.0
WO_3	41.39 ± 0.12	35.78 ± 0.09	34.68 ± 0.09	37.94 ± 0.09	36.81 ± 0.09	530.6 ± 0.1	-
WO_3-TiO_2 heterojunction	41.37 ± 0.06	35.75 ± 0.06	34.70 ± 0.06	37.87 ± 0.06	36.71 ± 0.02	530.6 ± 0.1	459.4 ± 0.1

Table S3. Relative fraction of W species in WO_3 and WO_3-TiO_2 heterojunction samples derived from component fitting of high-resolution W 4f XPS spectra. Listed are the mean ± deviation from one (with irradiation) or two (without irradiation) analysis points per sample, with two (TiO_2 and WO_3 samples) or four (WO_3-TiO_2) samples per sample type.

Sample	**%Area for W^{6+} contribution**	**%Area for W^{5+} contribution**	**Change in %Area induced by assembly for W^{5+} (%)**	**Change in %Area induced by irradiation for W^{5+} (%)**
WO_3 without irradiation	93.1 ± 0.7	3.1 ± 0.9	-	-
WO_3 with irradiation	91.7 ± 1.1	4.4 ± 1.3	-	**43.0**
WO_3-TiO_2 without irradiation	73.3 ± 1.6	7.6 ± 0.8	**144.7**	-
WO_3-TiO_2 with irradiation	70.3 ± 1.5	9.3 ± 0.8	-	**23.0**

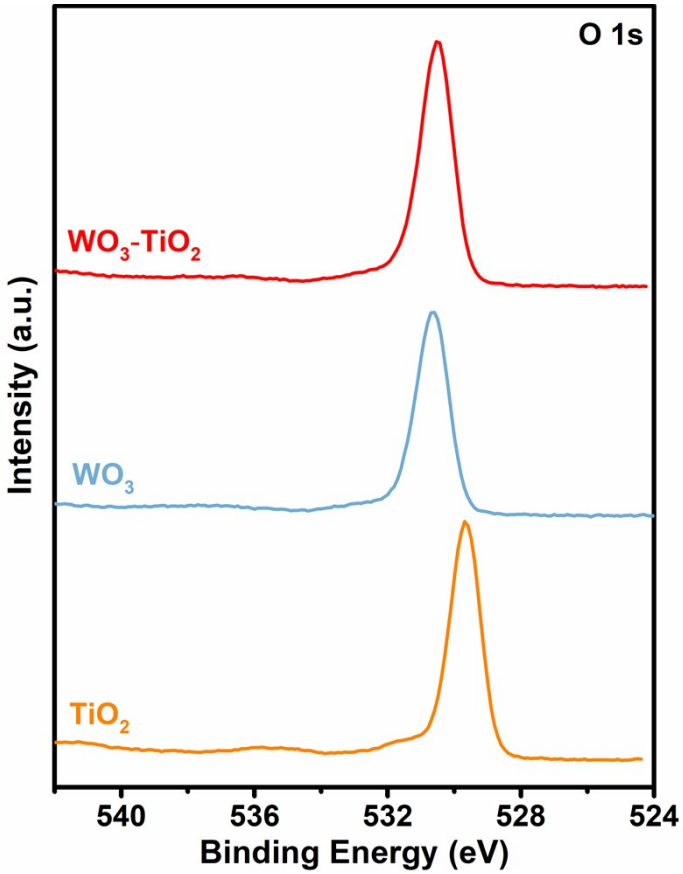

Fig. S1 Selected, representative high-resolution O 1s spectra from TiO_2, WO_3 and WO_3-TiO_2 heterojunction samples.

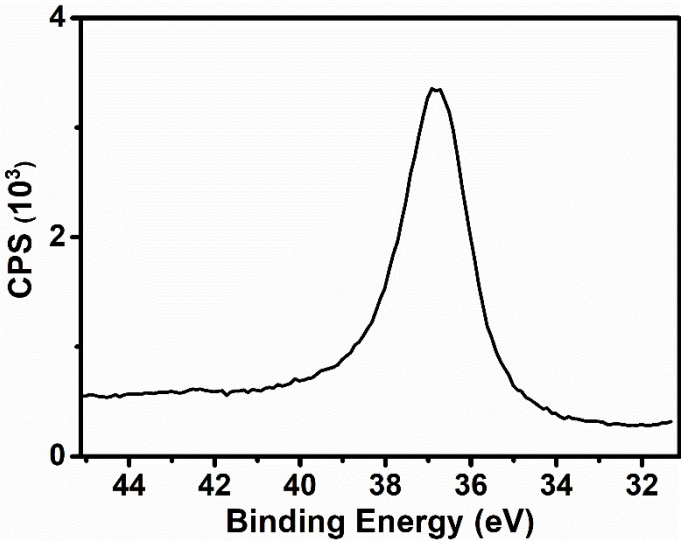

Fig. S2 Selected, representative high-resolution Ti 3p spectrum from the TiO_2 reference sample.

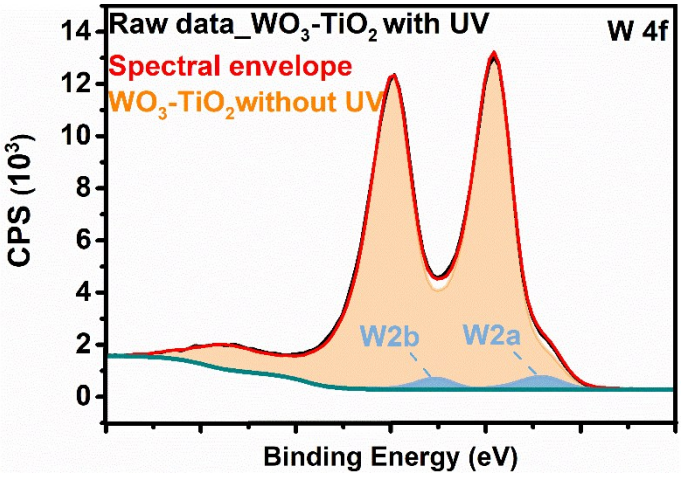

Fig. S3 Fitting of selected, representative W 4f spectra of the WO_3-TiO_2 heterojunction with irradiation using a model spectrum, specifically the experimental data of the same sample without irradiation. The remaining doublet W2 peaks is assigned to W^{5+}.

Characterization of the WO_3-TiO_2 heterojunction.

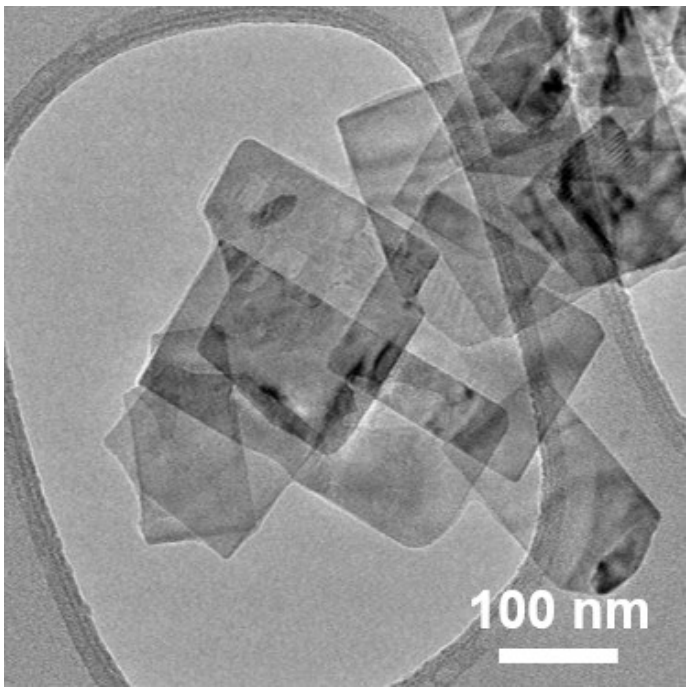

Fig. S4 TEM image of TiO_2 nanosheets synthesized by the growth control method.

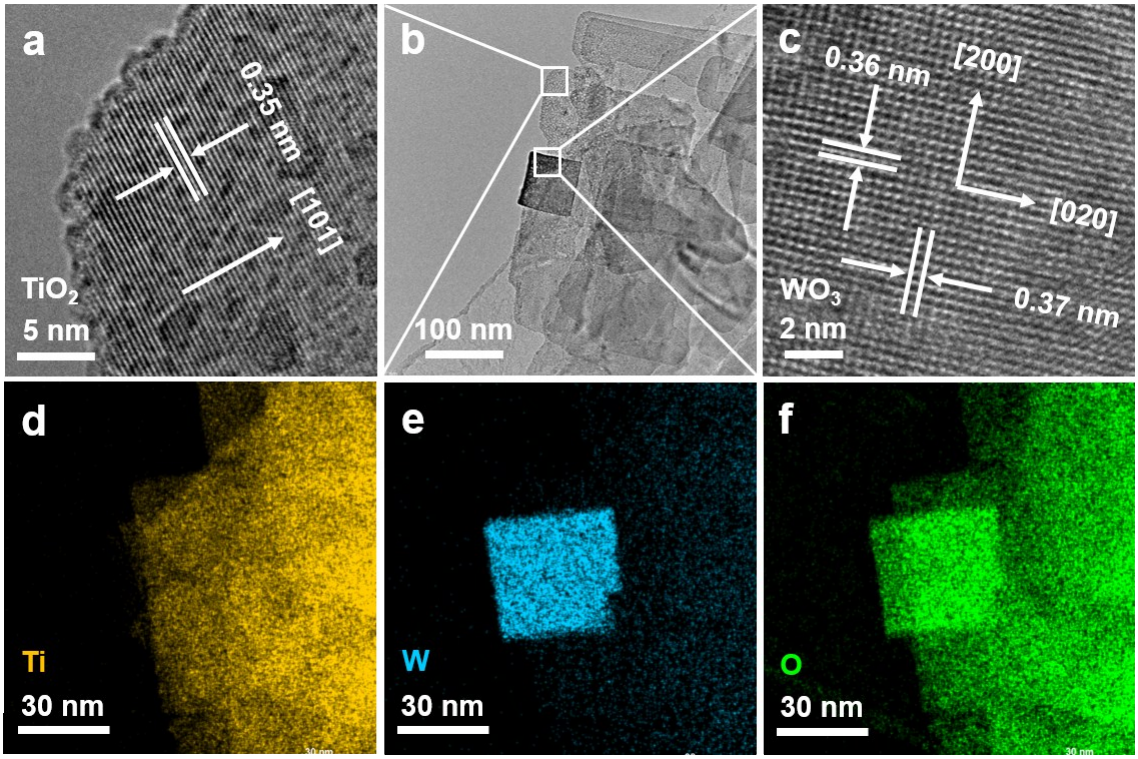

Fig. S5 (a-c) TEM, HRTEM and (d-f) EDX mapping images of the lateral surface of the WO_3-TiO_2 vertical heterojunction.

In **Fig. S5**a, the lattice recorded from the lateral surface of a TiO_2 nanosheet shows an interplanar distance of 0.35 nm which corresponds to {101} faces of anatase phase [15]. In **Fig. S5**c, the lattice distances of 0.36 and 0.37 nm of WO_3 could be assigned to the monoclinic-{200} and {020} planes respectively.[16]

Table S4. Zeta potential of the as-prepared TiO_2 nanosheets at pH = 2.

Time of repetition	1	2	3	Average
Zeta-potential (mV)	+ 21.6	+ 22.6	+ 21.5	+ 21.9 (± 0.61)

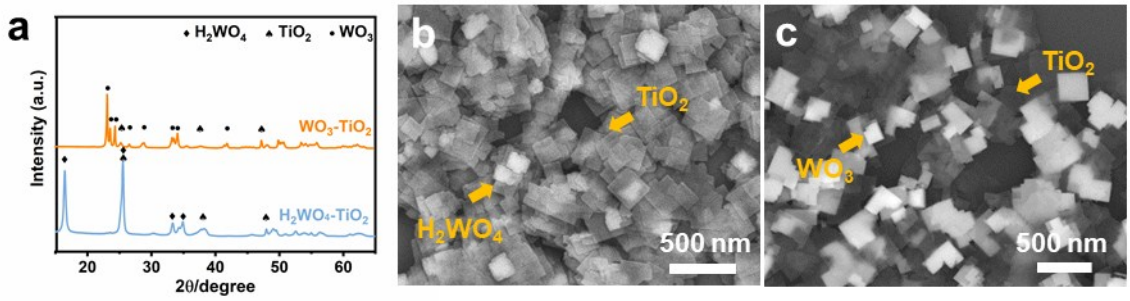

Fig. S6 Formation of H_2WO_4 and WO_3 nanosheets over TiO_2: (a) XRD spectra of the H_2WO_4-TiO_2 obtained after 14 h-hydrolysis (pH = 2) and WO_3-TiO_2 samples obtained from the following hydrothermal treatment at 180 ℃ for 4 h. SEM images of the (b) H_2WO_4-TiO_2 and (c) WO_3-TiO_2 samples presented in (a).

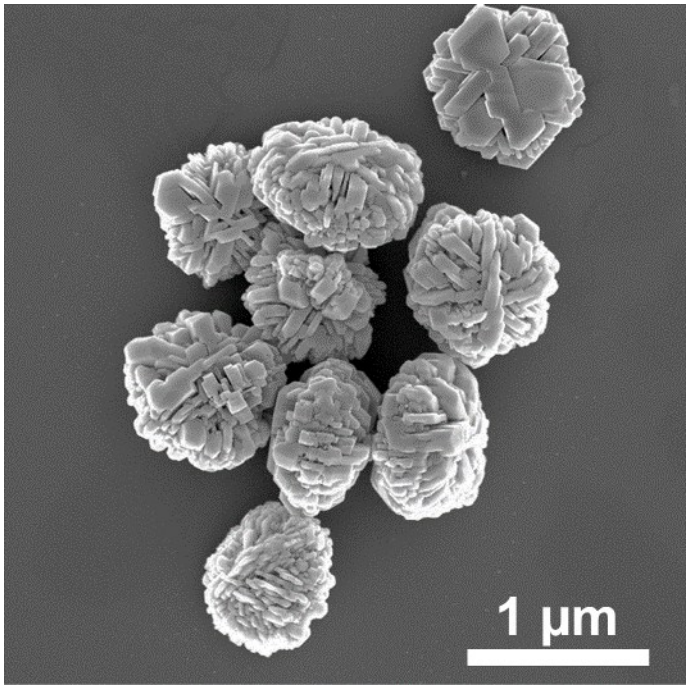

Fig. S7 SEM image of WO_3 fabricated in the absence of TiO_2 nanosheets.

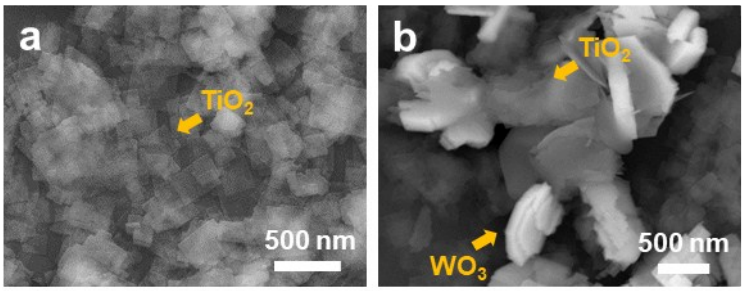

Fig. S8 SEM images of samples (a) obtained after 1 h-hydrolysis reaction and (b) that was further processed in hydrothermal reaction at 180 ℃ for 4 h.

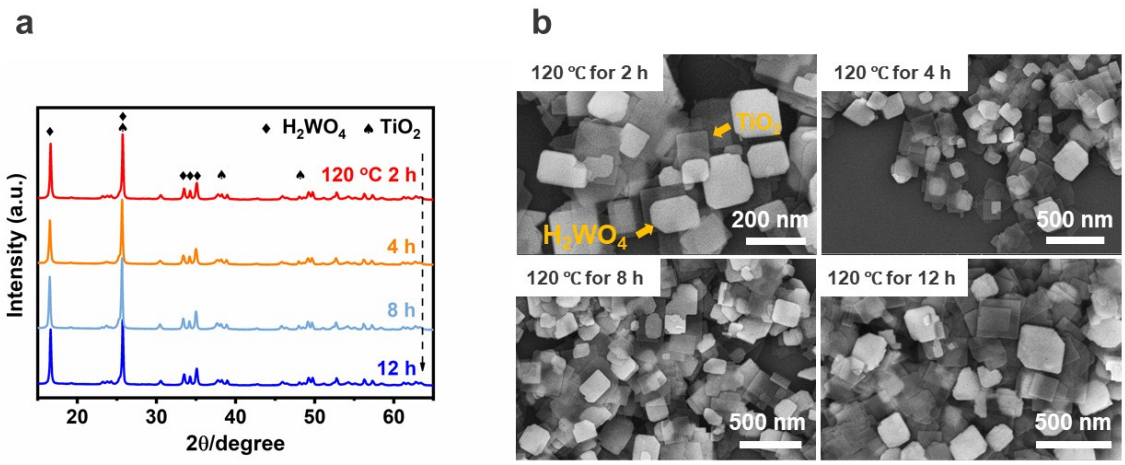

Fig. S9 (a) XRD patterns and (b) SEM images of H_2WO_4-TiO_2 samples obtained through hydrothermal treatment at 120 ℃ for different time.

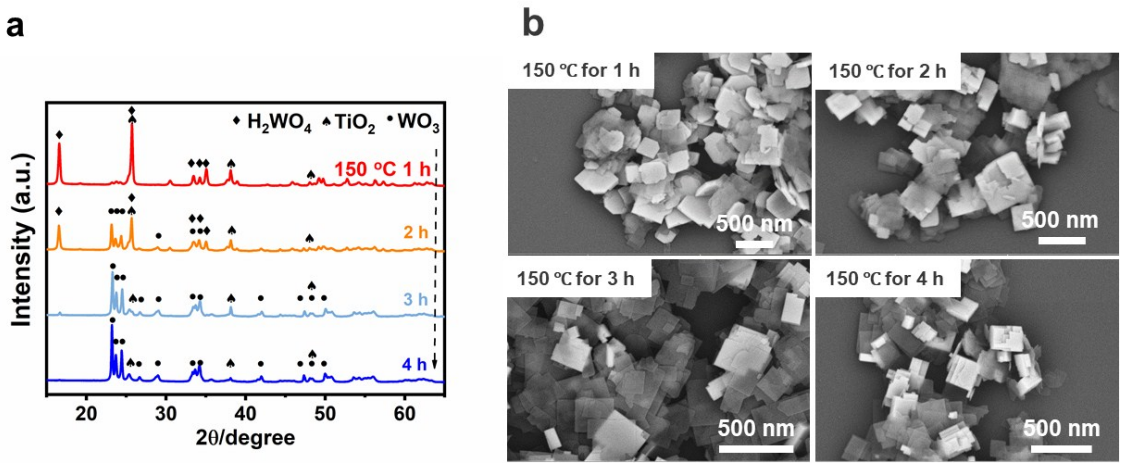

Fig. S10 (a) XRD patterns and (b) SEM images of H_2WO_4 (or WO_3)-TiO_2 samples obtained through hydrothermal treatment at 150 ℃ for different time.

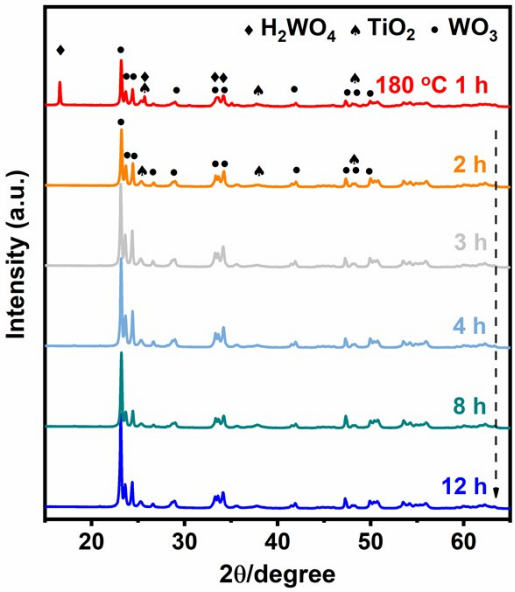

Fig. S11 XRD patterns of H_2WO_4 (or WO_3)-TiO_2 samples obtained through hydrothermal treatment at 180 ℃ for different time.

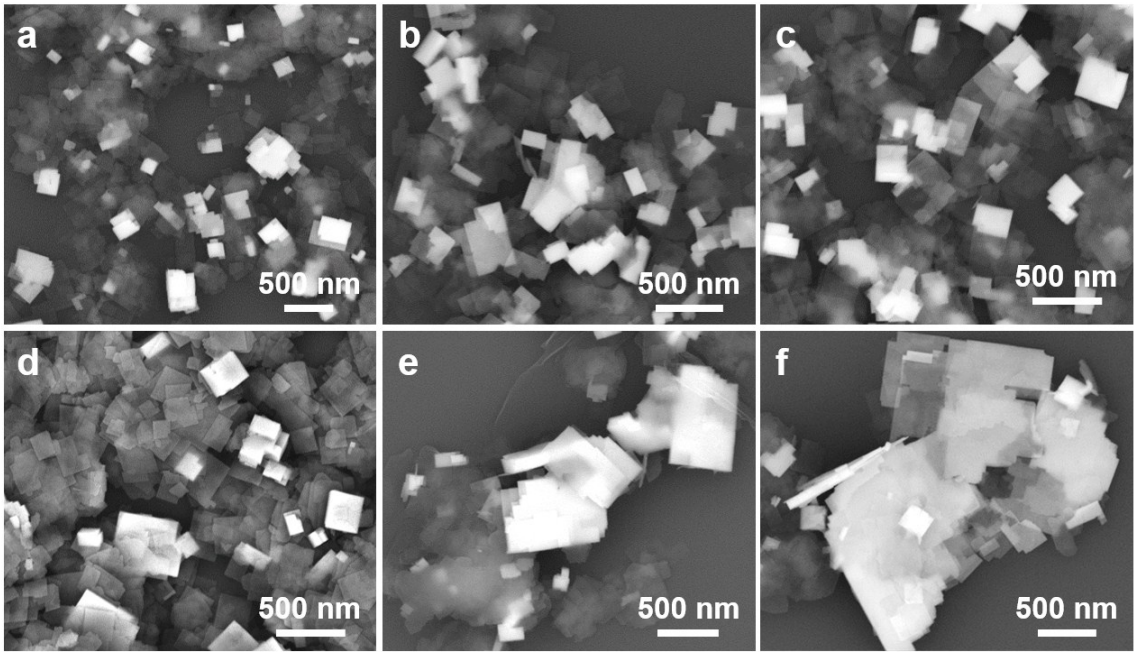

Fig. S12 SEM images of H_2WO_4 (or WO_3)-TiO_2 samples obtained through hydrothermal treatment at 180 ℃ for (a) 1 h, (b) 2 h, (c) 3 h, (d) 4 h, (e) 8 h and (f) 12 h.

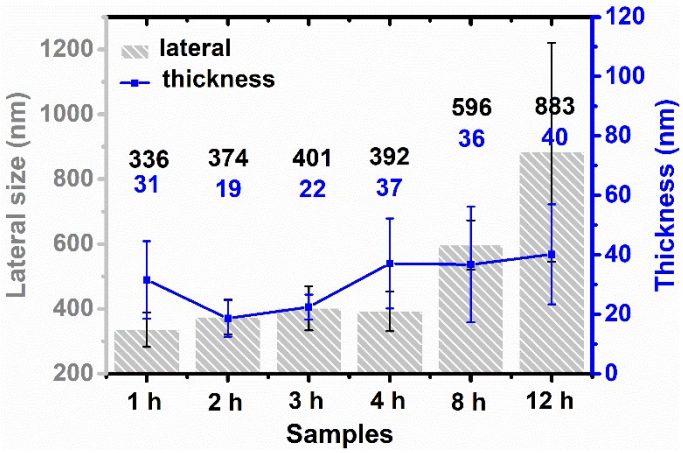

Fig. S13 The thickness and lateral sizes of WO_3 (or H_2WO_4) nanosheets synthesized at 180 ℃ for different treatment time. Error bar represents standard deviation from 20 analysis points.

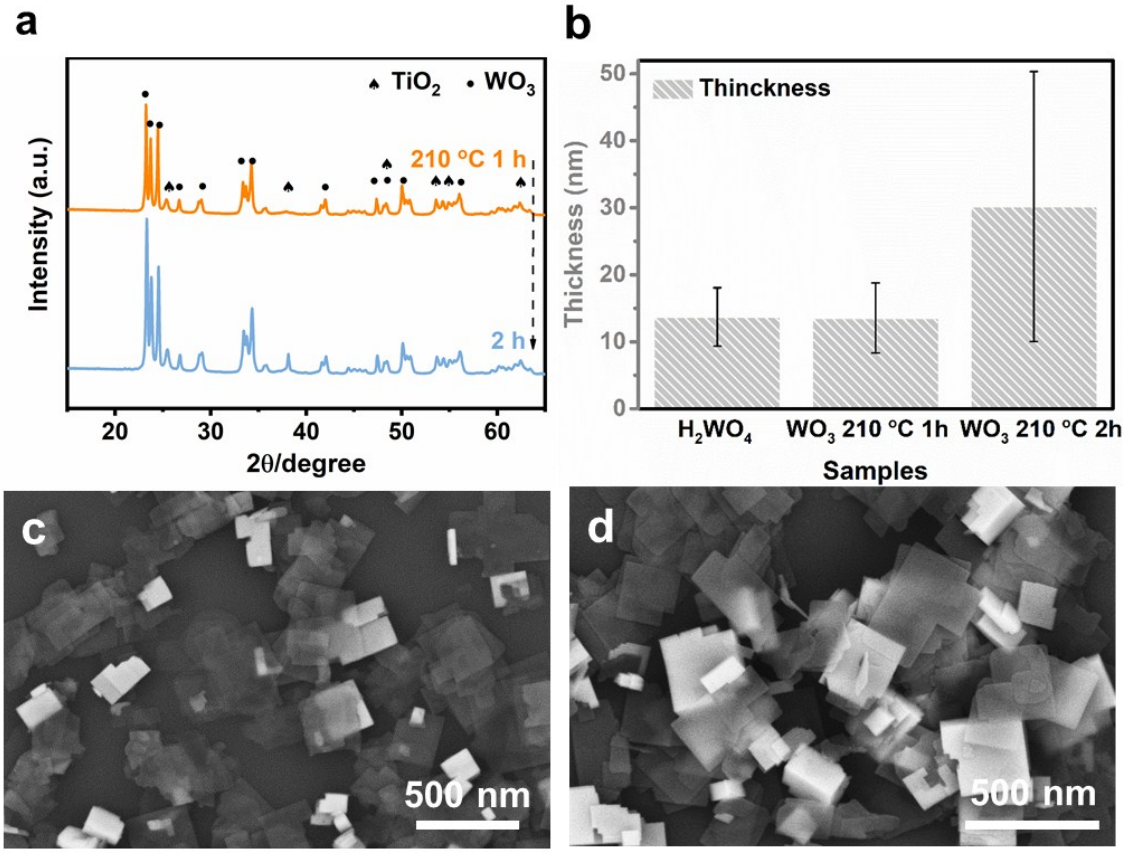

Fig. S14 (a) XRD patterns of WO_3-TiO_2 samples hydrothermally synthesized at 210 ℃; (b) Thickness of H_2WO_4 and WO_3 nanosheets that were in situ grafted on TiO_2 sheets. The WO_3 nanosheets were prepared through a further hydrothermal treatment at 210 ℃ compared with the H_2WO_4 sheets. Error bar represent standard deviation from 20 analysis points; SEM images of WO_3-TiO_2 heterojunction prepared via hydrothermal treatment at 210 ℃ for (c) 1 h and (d) 2 h.

Temperature and time of hydrothermal treatment have significant impacts on the morphology and crystallinity of the final WO_3-TiO_2 samples. As shown in **Fig. S9**, H_2WO_4 was still the dominant phase of tungsten for the samples prepared under 120 ℃ even though the treatment time was extended to 12 h. It demonstrates that 120 ℃ is not sufficient to drive the dehydration of H_2WO_4 forming WO_3. When the temperature was increased to 150 ℃, the shrinking of the H_2WO_4 diffraction intensity implied gradual decomposition of H_2WO_4 to WO_3 with increasing time (**Fig. S10**a). Almost all tungsten phase has transformed into WO_3 at the third hour. There was an obvious morphology variation, from regular, single-layer plate to thick and step-like structure (**Fig. S10**b), demonstrating that phase conversion was accompanied by crystal growth. The phase conversion was faster at 180 ℃. As shown in **Fig. S11**, the H_2WO_4 peaks disappear after 2 h-hydrothermal treatment, suggesting the completion of dehydration. Besides, there was a gradual coarsening of the WO_3 sheets in thickness and lateral size, although the phase transformation has terminated when the treatment time was extended from 2 h to 12 h (**Fig. S12** and **S13**). When the hydrothermal temperature was lifted to 210 ℃, one hour-treatment was sufficient to completely convert H_2WO_4 to WO_3 (**Fig. S14**a). The phenomenon confirms an accelerated phase conversion with rising temperature. According to **Fig. S14**b-d, the growth of WO_3 with a thickness of only 13.5 nm within 1 h hydrothermal treatment is negligible compared to its precursor, H_2WO_4 with an average thickness of 13.7 nm. This result reveals that the promptly completed phase transformation at high temperature could greatly confine the thickening period of WO_3, since the growth of WO_3 proceeds throughout the hydrothermal reaction.

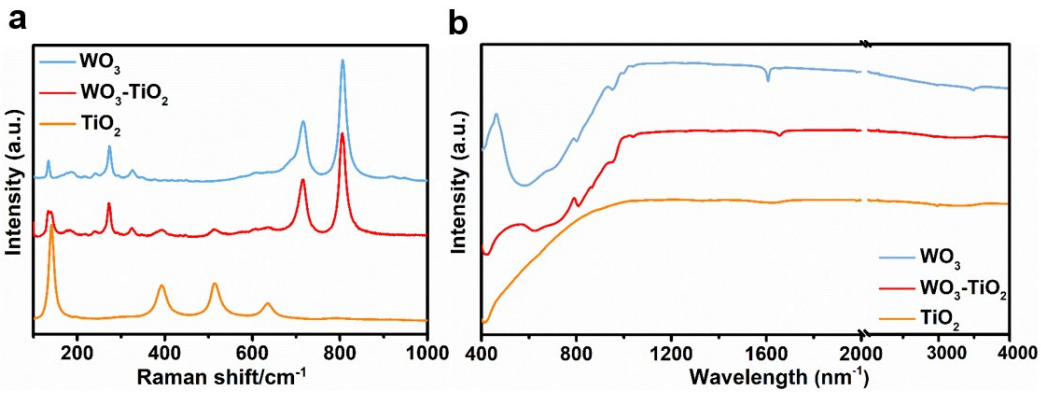

Fig. S15 (a) Raman and (b) FTIR spectra of pure WO_3, TiO_2 and the WO_3-TiO_2 vertical heterojunction.

In **Fig. S15**a, the peaks of TiO_2 at 197.3 cm^{-1}, 392.7 cm^{-1}, 514.0 cm^{-1} and 634.6 cm^{-1} show a typical spectrum of anatase structure.[17] Pure WO_3 exhibits the peaks at 134.4 cm^{-1} and 271.9 cm^{-1} that are assigned to bending vibration of W–O–W bond. Those at higher wave numbers of 716.6 cm^{-1} and 809.2 cm^{-1} are related to stretching vibration of oxygen in O–W–O.[18] The spectrum from WO_3-TiO_2 exhibits combined contributions of both TiO_2 and WO_3, revealing it a hybrid of both phases.

In the FTIR spectrum of **Fig. S15**b, the peak of TiO_2 at 424 cm^{-1} is assigned to Ti–O–Ti vibration and for WO_3 the broad peak in the range of 521-696 cm^{-1} could be attributed to the characteristic vibration of W–O and W–O–W. The additional peaks of all three samples at around 1600 cm^{-1} are due to the adsorbed water and –OH bond. The WO_3-TiO_2 also exhibits spectral features of both TiO_2 and WO_3.

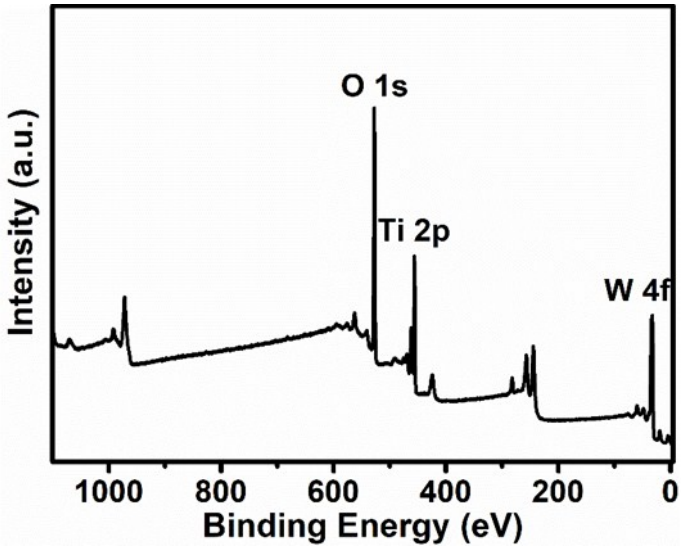

Fig. S16 Selected, representative XPS survey spectrum of the WO_3-TiO_2 heterojunction.

Table S5 Elemental quantification derived from XPS survey spectra expressed as atomic% of the WO_3-TiO_2 heterojunction. The residual fluorine might originate from hydrofluoric acid when the TiO2 nanosheets were prepared and the detected C element signal can be attributed to the adsorption of organic contamination, i.e. adventitious carbon.

Atomic%	Mean ± deviation
F 1s	0.65 ± 0.08
O 1s	60.29 ± 0.30
Ti 2p	17.13 ± 0.37
C 1s	13.06 ± 0.47
W 4f	8.87 ± 0.28

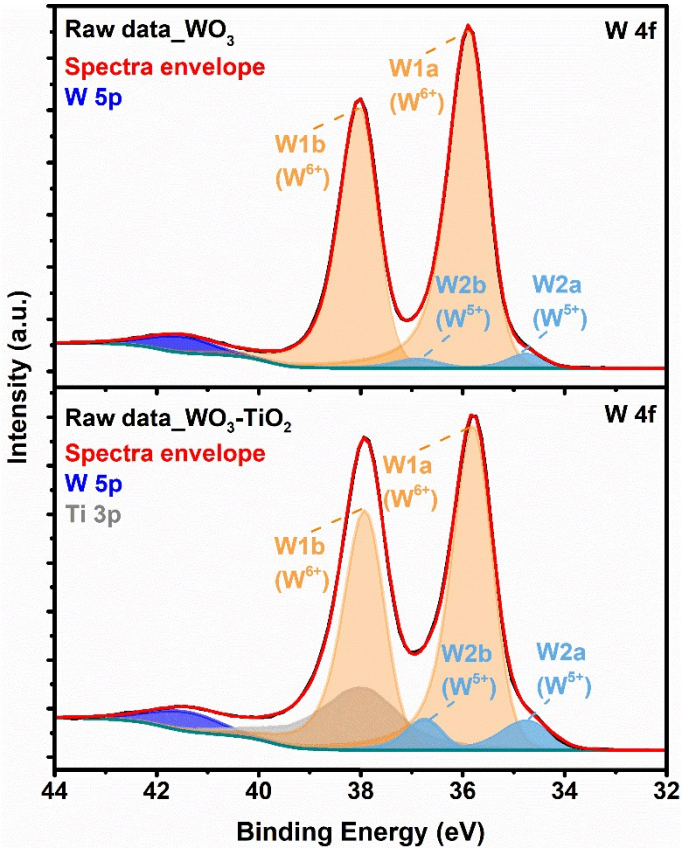

Fig. S17 High-resolution XPS fitting spectra of W 4f for WO_3 and the WO_3-TiO_2 heterojunction. An increase in W2 peaks (W2a and 2b) assigned to W^{5+} could be observed in WO_3-TiO_2 spectrum compared to WO_3 plot.

Z-scheme photocatalytic charge transportation route.

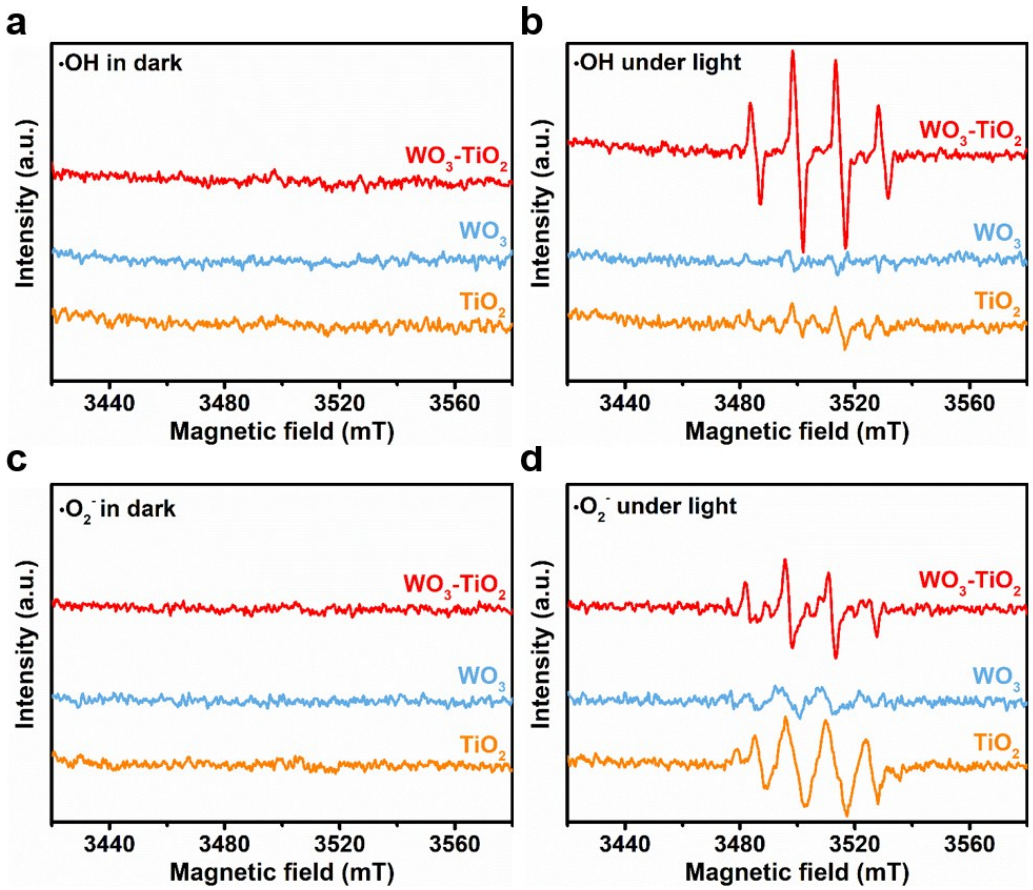

Fig. S18 EPR spectra of •OH generated by TiO_2, WO_3 and the WO_3-TiO_2 heterojunction (a) in dark and (b) under 10 min Xenon lamp irradiation. EPR signals of $•O_2^-$ (c) in dark and (d) under 10 min irradiation.

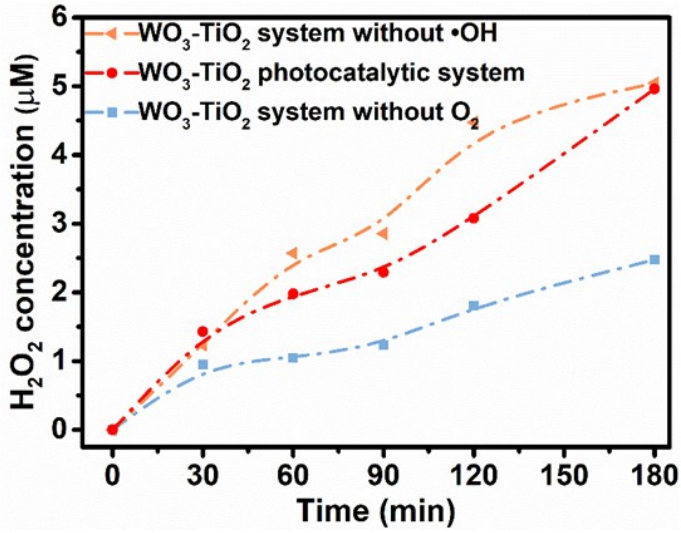

Fig. S19 The amount of H_2O_2 in the WO_3-TiO_2 photocatalytic system with isopropanol as •OH scavenger and N_2 purging to remove O_2.

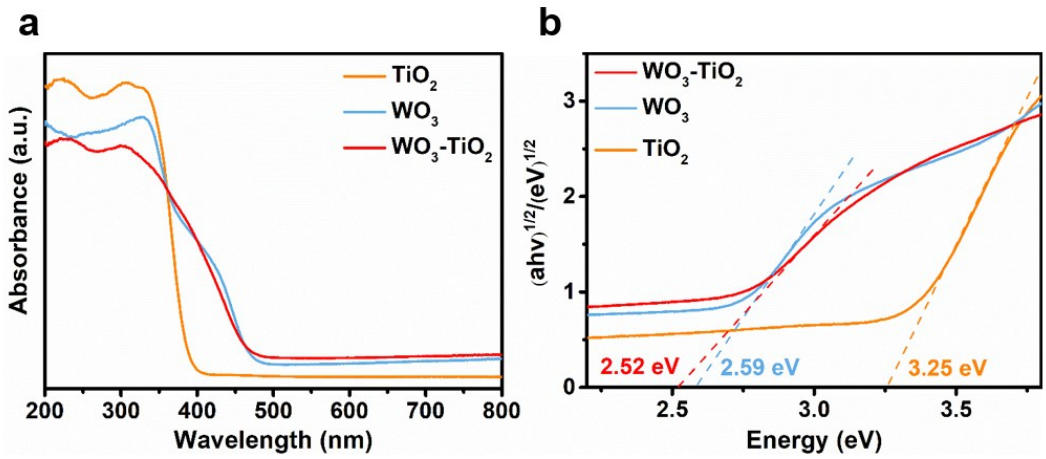

Fig. S20 (a) UV−vis diffuse reflectance spectra and (b) plots of the $(\alpha h\nu)^{1/2}$ versus photon energy of the photocatalysts.

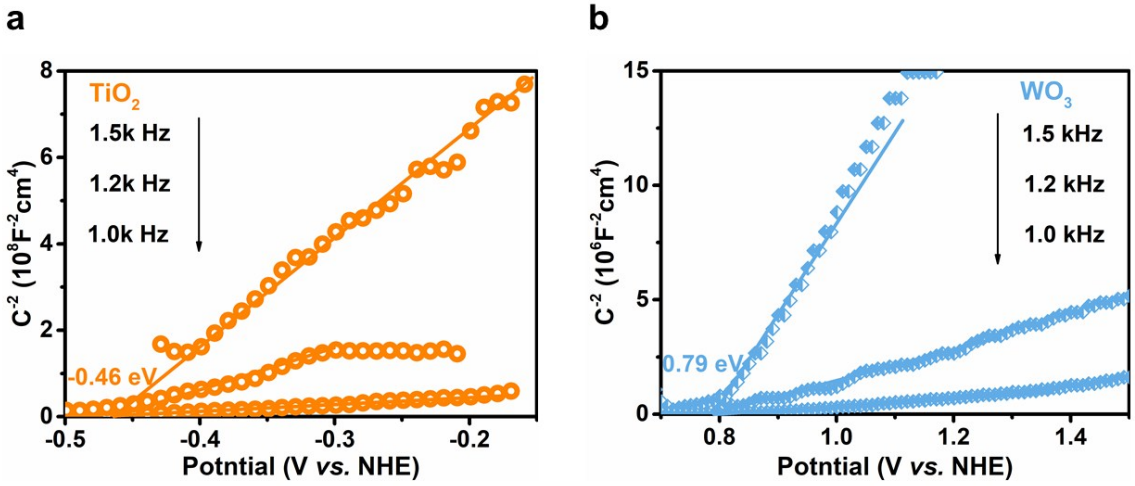

Fig. S21 Mott-Schottky plots of (a) TiO_2 and (b) WO_3.

The UV-vis diffuse reflectance spectra (DRS) plots in **Fig. S20** shows the light harvesting capacity and bandgaps of photocatalysts. The TiO_2 exhibits an absorption edge of around 380 nm corresponding to the band gap of 3.25 eV. WO_3 behaves better in visible light region with the absorption onset at 480 nm and a narrower band gap of 2.59 eV. The heterojunction, WO_3-TiO_2 retains the excellent visible light harvesting ability of WO_3 with a similar band gap value (2.52 eV).

The positive slopes of Mott-Schottky in **Fig. S21** suggest both TiO_2 and WO_3 as n-type semiconductors. The flat band positions of TiO_2 and WO_3 are measured to be -0.46 and +0.79 eV *vs.* HNE respectively. For n-type semiconductors, the CB edges are close to the values of flat band potentials.[19] The band structures of semiconductors could be analyzed with the following formula (Equation (1)), where E_g stands for the band gap value, E_{VB} is the VB potential and E_{CB} is the CB value.[20, 21] Thus, the CB values of TiO_2 and WO_3 are estimated to be -0.46 eV and +0.79 eV respectively, and the corresponding VB positions are located at +2.79 and +3.38 eV (**Table S6**).

$$E_{VB} = E_g + E_{CB} \qquad \text{Equation (1)}$$

Table S6 Bandgaps and band edge potentials of TiO_2 and WO_3.

Semiconductors	TiO_2	WO_3
Bandgap (eV)	3.25	2.59
CB edge potential (eV *vs.* NHE)	-0.46	+0.79
VB edge potential (eV *vs.* NHE)	+2.79	+3.38

Photocatalytic antibacterial performance.

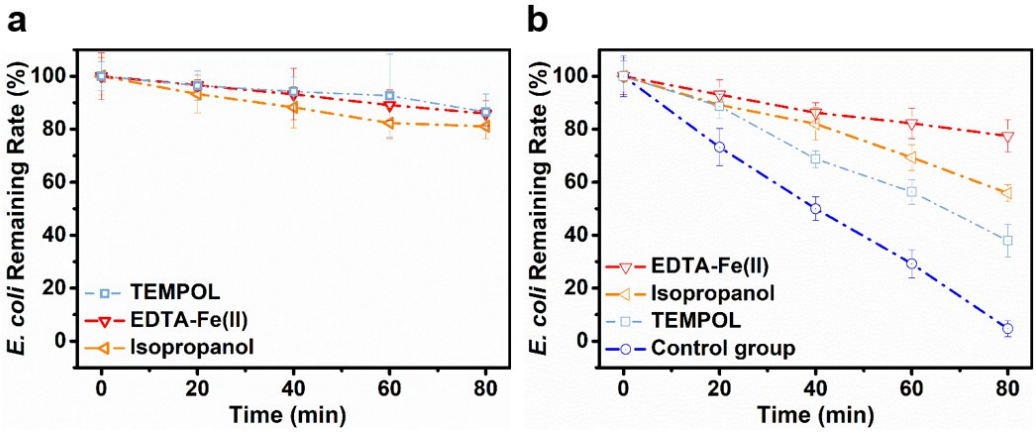

Fig. S22 *E. coli* survival rate with the existence of scavenger of individual ROS. (a) Control bacterial groups in the scavenger solution under constant illumination. The viable rate of above 80% implies that the used trapping reagents in given dosage have little toxic effect on E. coli cells; (b) the photocatalytic reaction system with the presence of both scavengers and WO_3-TiO_2.

References

1. D. R. Baer and I. S. Gilmore, *J. Vac. Sci. Technol. A* 2018, **36**, 068502.
2. T. L. Barr and S. Seal, *J. Vac. Sci. Technol. A* 1995, **13**, 1239-1246.
3. P. Swift, *Surf. Interface Anal.* 1982, **4**, 47-51.
4. *NIST X-ray Photoelectron Spectroscopy Database, NIST Standard Reference Database Number 20, National Institute of Standards and Technology, Gaithersburg MD*, 2000, **20899**, doi: 10.18434/T4T88K, accessed: 2 April 2019.
5. M. C. Biesinger, L. W. M. Lau, A. R. Gerson and R. S. C. Smart, *Appl. Surf. Sci.* 2010, **257**, 887-898.
6. P. M. A. Sherwood, *Surf. Interface Anal.* 2019, **51**, 589-610..
7. C. D. Wagner and G. E. Muilenberg, *Handbook of X-ray Photoelectron Spectroscopy: A Reference Book of Standard Data for Use in X-ray Photoelectron Spectroscopy*, Perkin-Elmer, 1979.
8. G. Beamson and D. Briggs, *High Resolution XPS of Organic Polymers: The Scienta ESCA300 Database*, Wiley, 1992.
9. N. Fairley, *CasaXPS: Processing Software for XPS, AES, SIMS and More, see www.casaxps.com, accessed: 2 April 2019*.
10. M. Biesinger, *X-ray Photoelectron Spectroscopy (XPS) Reference Pages, see http://www.xpsfitting.com/, accessed: 2 April 2019*.
11. N. Fairley, C. S. Ltd and C. S. L. Staff, *CasaXPS Manual 2.3.15: Introduction to XPS and AES*, Casa Software, Limited, 2009.
12. S. Tougaard, *Surf. Interface Anal.* 1997, **25**, 137-154.
13. J. Walton, M. R. Alexander, N. Fairley, P. Roach and A. G. Shard, *Surf. Interface Anal.* 2016, **48**, 164-172.
14. C. D. Easton, A. J. Bullock, G. Gigliobianco, S. L. McArthur and S. MacNeil, *J. Mater. Chem. B* 2014, **2**, 5558-5568.
15. J. S. Chen and X. W. Lou, *Mater. Today* 2012, **15**, 246-254.
16. J. Zhang, P. Zhang, T. Wang and J. Gong, *Nano Energy*, 2015, **11**, 189-195.
17. H. Khan and D. Berk, *Appl. Catal. A* 2015, **505**, 285-301.
18. I. M. Szilágyi, B. Fórizs, O. Rosseler, Á. Szegedi, P. Németh, P. Király, G. Tárkányi, B. Vajna, K. Varga-Josepovits, K. László, A. L. Tóth, P. Baranyai and M. Leskelä, *J. Catal.* 2012, **294**, 119-127.

19. Q. Ruan, W. Luo, J. Xie, Y. Wang, X. Liu, Z. Bai, C. J. Carmalt and J. Tang, *Angew. Chem. Int. Ed.* 2017, **56**, 8221-8225.
20. L. J. Zhang, S. Li, B. K. Liu, D. J. Wang and T. F. Xie, *ACS Catal.* 2014, **4**, 3724-3729.
21. S. Cao, B. Shen, T. Tong, J. Fu and J. Yu, *Adv. Funct. Mater.* 2018, **28**, 1800136.